Available online at www.sciencedirect.com
ScienceDirect
International Journal of Thermal Sciences 45 (2006) 1052–1065
International Journal of Thermal Sciences
www.elsevier.com/locate/ijts

Improvements of the base bleed effect using reactive particles

Hervé Bournot [a,*], Eric Daniel [a], Roxan Cayzac [b]

[a] *Polytech' Marseille, IUSTI UMR CNRS 6595, 5, rue E. Fermi, Technopôle de Château Gombert, 13453 Marseille cedex 13, France*
[b] *Giat Industries, 7, Route de Guerry, F-18023 Bourges cedex, France*

Received 30 September 2005; received in revised form 11 January 2006; accepted 27 January 2006

Abstract

A numerical study of the base drag reduction of axisymmetric body projectiles in supersonic flight using a base bleed injection is presented in this paper. Unsteady computations of compressible viscous flow have been achieved in order to investigate the coupled effect of the bleed temperature and the bleed mass flow rate on the base pressure. The idea developed in the study, consists in the addition of metallic particles in the propellant composition used to provide the additional mass injected in order to obtain the lowest base drag. Indeed, for a low mass addition, a significant increase of the mixture energy is expected due to the particles combustion. Base flow with reactive two-phase injection is then simulated. Results show the ability of the method to describe such flows and the efficiency of the particles combustion to increase the base bleed reducing drag effect.

Keywords: Base flow; Base bleed; Two-phase; Compressible flow; Aluminum combustion

1. Introduction

Reducing the drag acting on a supersonic projectile is a challenging task. During flight, the low pressure in the afterbody region is responsible for up to 50% of the total drag. Reducing the base drag is an efficient and practical way to reduce the total drag of the projectile. Two methods of drag reduction are typically employed. The first way is to optimize the shape of the projectile, typically through the use of a boattailed afterbody which reduces the base surface area exposed to the afterbody expansion. The second method consists of increasing the pressure behind the projectile. This can be accomplished with injection of a low velocity fluid in the recirculation region directly behind the base, otherwise known as base bleed. Due to the relatively low mass injection rates, the amount of thrust produced by the base bleed injection is negligible, especially when compared with high thrust rocket motors used on rocket-assisted projectiles. Base bleed is particularly effective for long range flights, where the integrated effect of the drag reduction is manifested. Such a capability is of significant current interest.

The detailed knowledge of the flow around the projectile, and particular the afterbody flow is a requirement before proposing solutions to reduce the drag. Hence, numerous papers can be found in the literature concerning experimental [1–7], theoretical [1–3,8] and—since the eighties—numerical studies [9–14].

Basic studies consider a simplified problem of a cylindrical projectile in a supersonic flow. The main characteristics of the afterbody flow are depicted at the top of Fig. 1. The flow is characterized by a low pressure recirculating region at the base, also called "dead air region". The recirculation is separated from the external flow by a stream line starting from the base corner, point A, and ending on the symmetry axis at the stagnation point, point B. An expansion fan is centered on the base corner because of the streamlines curvature induced by the separation mechanism. Downstream, the streamlines convergence at the stagnation point leads to recompression waves: the upstream pressure value is recovered. The mixing layer which exists along the streamline (AB) turns into a trailing wake after it has crossed the recompression waves.

* Corresponding author.
E-mail addresses: herve.bournot@polytech.univ-mrs.fr (H. Bournot), eric.daniel@polytech.univ-mrs.fr (E. Daniel), r.cayzac@giat-industries.fr (R. Cayzac).

1290-0729/$ – see front matter
doi:10.1016/j.ijthermalsci.2006.01.018

Nomenclature

S_{base}	base surface ..... m^2	Q_{g-p}	convective heat transfer between the gaseous and the dispersed phase
p_c	average base pressure ..... Pa	$\dot{\omega}_{p,i}$	mass transfer within the dispersed phase
p	static pressure ..... Pa	$\dot{\Gamma}_{g-p}$	mass transfer between the gas and the particles due to the aluminum combustion
T	temperature ..... K	Γ_{energ}	heat released by the combustion of aluminum particles
ρ	density of the considered phase ..... kg m^{-3}		
$\vec{T}_p$	pressure drag (or shape drag) ..... N	*Subscript*	
I	injection parameter, $= \dot{m}/(\rho_0 U_0 S_{\text{base}})$		
$\dot{m}$	injection mass flow rate ..... kg m^{-3}	0	relative to the upstream flow
$\vec{U}$	velocity vector of the considered phase	bb	relative to the base bleed injection
N	density number of particles ..... m^{-3}	g	relative to the gaseous phase
ε	energy of the considered phase	p	relative to the particles (dispersed phase)
$\vec{F}_{g-p}$	momentum transfer between the gaseous and the dispersed phase due to particles drag		

The pressure drag (or shape drag), $\vec{T}_p$, is defined by the integral of pressure force applied on the body projectile: $\vec{T}_p = \int_S -p\vec{n}\,\mathrm{d}S$. Considering the base, the lower the pressure acting on the base is, the higher the base drag is.

Considering the boattail effect (Fig. 1, middle), it first decreases the base surface, and so diminishes effects of the low base pressure. Secondly, since the radial component of the flow is non-zero upstream of the base, the boat tail decreases the strength of the expansion fan centered on the base corner. The higher base pressure is manifested by an increase of the recirculation length. The boattail also decreases entrainment in the mixing layer [5].

Considering the base bleed effect, the flow pattern is changed as depicted at the bottom of Fig. 1. The recirculating flow (now labeled PRR for Primary Recirculating Region) has moved downstream due to the motion of the injected gases. Bleed gases escape from the bleed section between the PRR and the external supersonic flow and create a secondary recirculating region (labeled SRR) against the annulus surface of the base. The recirculation is now separated by a stream line starting and ending on the symmetry axis. There are two distinct mixing layers: the external mixing layer (between the PRR and the external supersonic flow), and the bleed jet mixing layer (between the bleed jet and the SRR, on the edge of the bleed jet).

In the present study, the base bleed effect is considered. In actual system, the mass flow rate injected in the afterbody flow is provided by the combustion of a propellant. It is important to notice that the injection of mass has not a rocket effect. Actually, three regimes for base bleed injection are observed according to the experimental and theoretical studies from the 1950's [1,8]. This description is based on the amount of injected mass:

- In regime I, the injected fluid provides a portion of the mass required for the mixing layer entrainment process. The PRR decreases in strength with the injection rate, the recompression shock is weakened, and the base pressure increases approximately linearly.
- Regime II starts when the bleed flow rate is sufficient to provide all the fluid required by the mixing entrainment process. At this point, the recompression shock is considerably weakened, and the base pressure reaches a maximum value. As the bleed rate is increased, the wake opens because the bleed jet contains enough momentum to penetrate through the primary recirculation region.
- Regime III is reached as the bleed rate is increased even further, and eventually leads to power-on conditions. The bleed flow acts as a highly underexpanded jet and the base pressure increases with the bleed flow rate. This regime is not used for base bleed applications.

The optimal mass injection rate value for base bleed is located at the transition between regime I and regime II (see Fig. 2).

In numerical studies on afterbody flows with or without base bleed, one can note that most of the latest references are focused on the turbulent aspects [9,10,12,15,16]. Nevertheless, turbulence modelling for base flow is not yet a resolved problem [17] even if some LES modelling has improved the quality of the agreement with experiments [18].

Kaurinkoski [19,20] and also Rose et al. [21,22] investigated base bleed configurations with special emphasis on the effect of chemical reaction between the bleed gases and the external air flow (post-combustion).

The combustion products temperature appear to be a very important parameter in the base bleed effect. It was shown that for the same external flow conditions, hot bleed gases lead to higher base pressure because of volumetric effects [2].

We will demonstrate that a possible way to obtain hot gases consists in the addition of metal particles in the propellant (aluminum particles). The energy released in the core flow or in the jet by the combustion of the metal particles will reduce the drag: this combustion is an energy source for the external flow. A very few work has been done in this way. In [23], the authors have shown that combustion of metal particles allows a post-combustion benefic for base bleed. In these experiments,

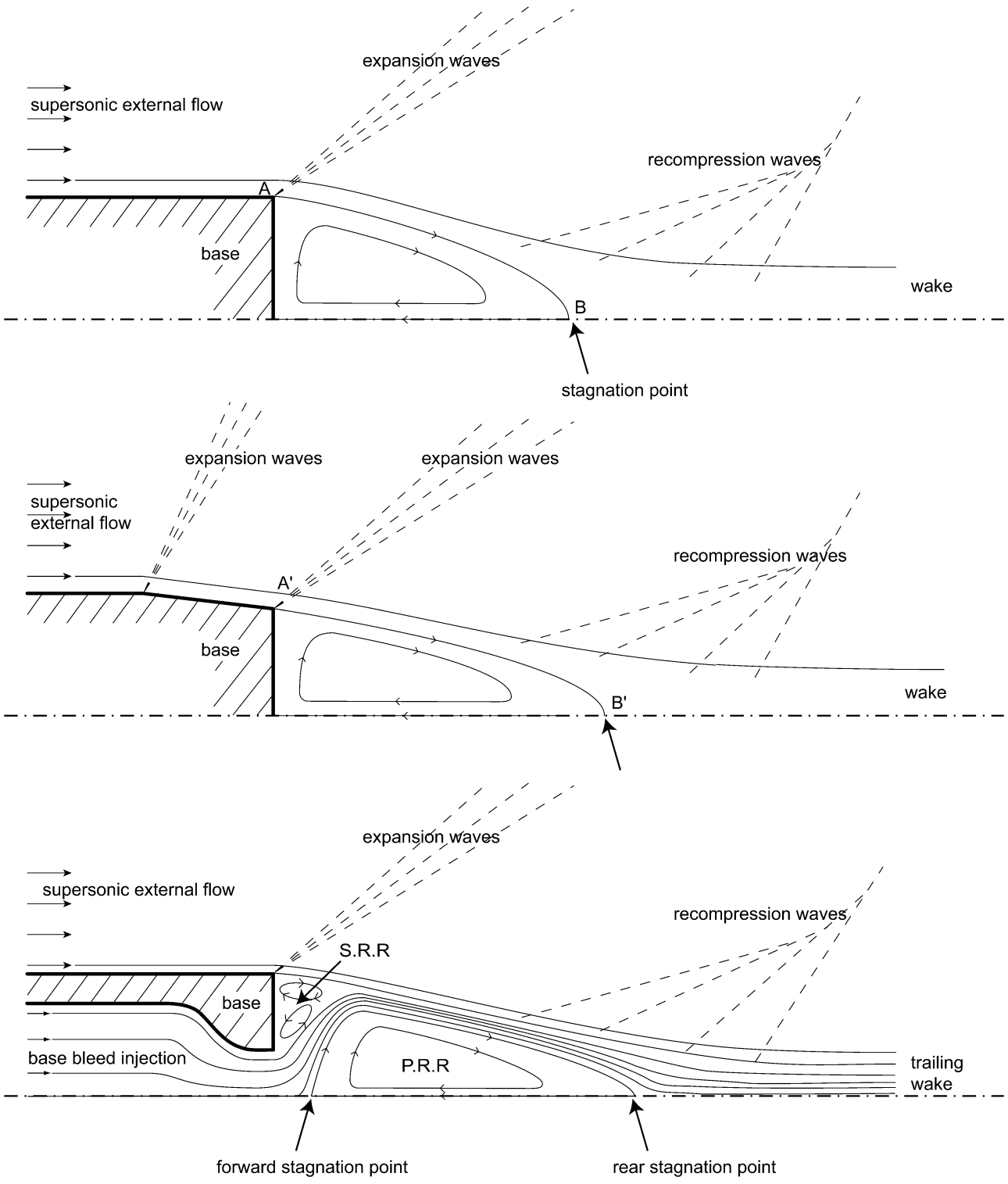

Fig. 1. Scheme of a blunt afterbody base flow (top), a boattailed afterbody flow (middle) and a base flow with base bleed (bottom).

magnesium has been chosen over aluminum because of higher energetic properties of magnesium. Nevertheless, aluminum particles are largely used in the formulation of propellants and some numerical investigations are necessary to understand such a complex system.

The paper is organized as follow. In a first part, the governing equations are reminded. It will be assumed that the unsteady compressible two-phase flow equations take into account the combustion of aluminium particles. The governing equations are based on a dilute two-phase flows assumptions.

Then, the flow simulations are presented and largely detailed. The results will show that hot gases reduce the drag. Then, the best way to obtain hot gases is to include some reactive particles in the propellant formulation.

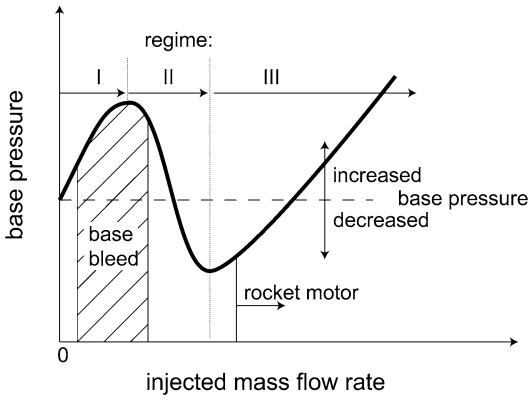

Fig. 2. Base pressure vs. injected mass flow rate.

2. Governing equations

The combustion of propellant inside the projectile provides the base bleed and induces a mixture of compressible flows and metal particles. Consequently, a multi-phase model is necessary to describe the flow in the afterbody region. This model must also describe the one-phase flow around the projectile. The flow may present some quasi-steady characteristics (mixing layers, vortex shedding) then an unsteady model for viscous compressible two-phase dilute flows is considered. The gaseous phase is described by the typical Navier–Stokes equations system. The dispersed phase dynamics is described by an Eulerian approach. The effects of the combustion of metallic particles are here investigated. It was successfully proven that the specific combustion of aluminum particles can be included in general codes devoted to Solid Rocket Motors flows [24].

The two-phase flow equations are hereafter reminded. More details about this complete model can be found in [24,25]. The particles phase (dispersed phase) as well as the gaseous phase are described by a set of partial differential equations representing the mass, momentum and energy conservation laws. The volume fraction of the solid phase is low enough to use a dilute flow assumption.

Gaseous phase equations

$$\frac{\partial \rho_g \vec{U}_g}{\partial t} + \vec{\nabla}.(\rho_g \vec{U}_g \vec{U}_g + p\bar{\bar{I}}) - \vec{\nabla}.\bar{\bar{\tau}}_v = \vec{F}_{g-p} + \Gamma_m \vec{U}_p \quad (1)$$

$$\frac{\partial \rho_g \varepsilon_g}{\partial t} + \vec{\nabla}.\big(\vec{U}_g[\rho_g \varepsilon_g + P]\big) - \vec{\nabla}.(-\vec{q} + \vec{U}_g.\bar{\bar{\tau}}_v) = \vec{F}_{g-p}.\vec{U}_p + \Gamma_{\text{energ}} + Q_{q-p} \quad (2)$$

$$\frac{\partial \rho_{g,i}}{\partial t} + \vec{\nabla}.\rho_{g,i}\vec{U}_g = \dot{\Gamma}_{p-g,i} \quad (3)$$

with $\sum \rho_{g,i} = \rho_g$ and $P = \rho_g R T_g$.

Dispersed phase equations

$$\frac{\partial \rho_p \vec{U}_p}{\partial t} + \vec{\nabla}.\rho_p \vec{U}_p \vec{U}_p = -\vec{F}_{g-p} - \Gamma_m \vec{U}_p \quad (4)$$

$$\frac{\partial N}{\partial t} + \vec{\nabla}.N\vec{U}_p = 0 \quad (5)$$

$$\frac{\partial \rho_p \varepsilon_p}{\partial t} + \vec{\nabla}.\rho_p \varepsilon_p \vec{U}_p = -\vec{F}_{g-p}.\vec{U}_p - \Gamma_{\text{energ}} - Q_{q-p} \quad (6)$$

$$\frac{\partial \rho_{p,i}}{\partial t} + \vec{\nabla}.\rho_{p,i}\vec{U}_p = -\dot{\Gamma}_{p-g,i} + \dot{\omega}_{p,i} \quad (7)$$

with $\rho_{p,i} = \rho_{\text{Al}}$ or $\rho_{\text{Al}_2\text{O}_3}$.

Both systems are coupled by source terms representing the particle/gas drag effect $\vec{F}_{g-p}$, the convective heat transfer between inert (alumina particles) and gas Q_{g-p}, and the heat released by the combustion of aluminum particles Γ_{energ}. One can notice two species equations for the solid phase: they represent the evolution of the aluminum mass and the alumina mass. Indeed, during the combustion, the aluminum particles evaporate and burn: one part of the combustion products goes into the gaseous phase as smoke of gaseous products; an other part is condensing at the surface of the particle. Thus, the combustion of metal particles is characterized by the presence of a residual particle of the metal oxide at the end of the combustion. This phenomenon, and also the fact that the break-up or coalescence phenomena are omitted, is the reason why there is global conservation of the density number of particles and thus no right-hand side term in Eq. (5). The mass transfer within the dispersed phase is modeled through the term $\dot{\omega}_{p,i}$ while $\dot{\Gamma}_{p-g,i}$ represent the mass transfer between the gas and the particles due to the aluminum combustion. The model we use for the aluminum combustion is a development of the Law's model (1973) that was presented in [24,25].

3. Numerical solution

In the research code [24,26,27] used in this study, the set of governing equations of the two-phase flow is solved by using a high order finite volume method. The different fluxes for the gaseous and dispersed phase are obtained with the solution of exact Riemann solvers [26,28]. The method is based on an explicit time integration. The boundary conditions are set by classical methods based on the integration of locally 1D relations chosen according to the incoming or outcoming waves.

Considering the initial conditions, base bleed simulations are started from the solution of a no-bleed case computation where the base bleed inlet condition is assumed to be a wall.

The specific flows encountered here involve boundary layers as well as Kelvin–Helmolthz instabilities that require a fine spatial resolution. A multi-domains approach allows maintaining a good numerical accuracy by using quadrangle cells and efficient parallel algorithm: in each domain, the set of equations is solved on a single processor; the connecting values are exchanged by using some MPI procedures.

In the following simulations, the mesh represents a simple cylindrical base. A cavity in the projectile body represents the combustion chamber and is numerically solved. The combustion of the propellant is modeled as an inlet boundary condition, for which the temperature and the mass flow rate are imposed. Computations are made on three grids: the first one (grid 1) is coarse, for a first approach, and consists of half as many points in each direction as the second (grid 2) which has 55 000 cells; for grid 2, the cell size is 5×10^{-2} mm at the wall. The third

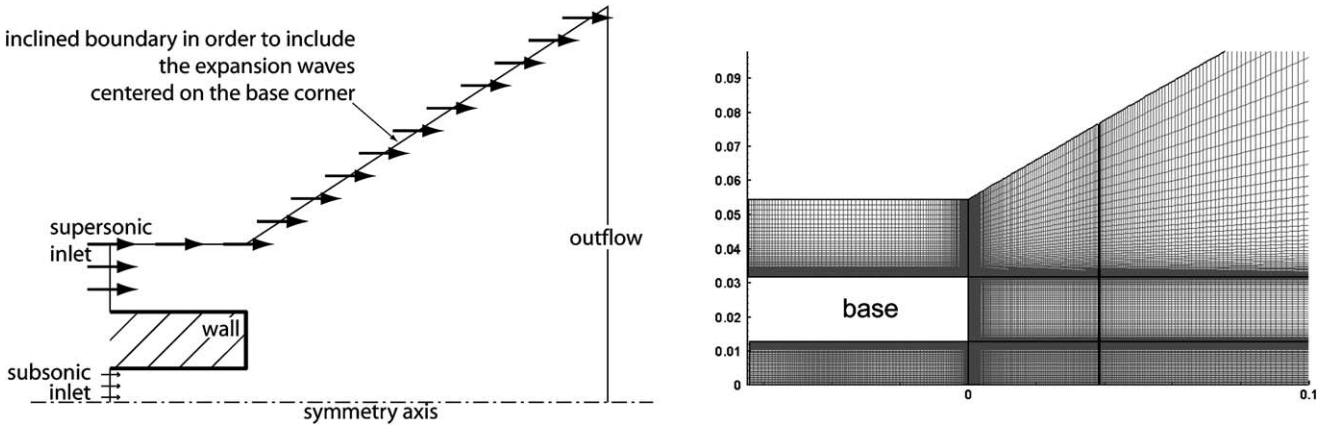

Fig. 3. Left: boundary conditions. Right: zoom of grid 2 (55 000 cells).

grid has twice as many points in each direction as the second and the cell size is 2.5×10^{-2} mm at the wall. A zoom of the near base region for grid 2 is shown in Fig. 3 (some domains are also visible). The mesh is designed to include the expansion waves generated at the detachment point i.e. the base corner.

4. Results

Results are presented as follow. Recent experiments on base flows with a gaseous base bleed injection are chosen as a case of reference and, as the conditions of these experiments are the baseline of the studies presented later, they are detailed first. This allows us to introduce the important parameters needed, the methodology adopted, and also the post-treatment applied to our numerical results. The ability of our computations to describe correctly the transition between the different flow regimes is also shown.

Then, the conditions of the case of reference are extended in order to investigate different aspects of the base bleed injection.

In the first place, a gaseous one-phase base bleed injection is still considered, but a parametric study on the influence of both bleed mass flow rate and bleed temperature is investigated. In the second place, the base bleed injection of a two-phase reactive mixture is considered. One specific case—chosen from results of the previous parametric study—is computed considering reactive particles added to the injection. Results are largely detailed; combustion effects are analyzed as the corresponding non-reactive two-phase injection case has also been computed.

4.1. Definition of the case of reference

The base bleed experiments investigated by Mathur and Dutton [6,7,29] are chosen as a reference. The flow behind a 63.5 mm diameter circular cylinder aligned with a Mach $M_0 = 2.45$ supersonic air flow is considered (the corresponding unit Reynolds number is $Re = \frac{U}{\nu} = 52 \times 10^6$ m^{-1}). The base bleed injection is made through a 0.4 diameter bleed orifice. The gas, both for external supersonic flow and base bleed injection is air. The total temperature of the bleed flow is $T_{\mathrm{bb}} = 300$ K and the bleed mass flow rate values are chosen to range regime I and regime II.

For the injection mass flow rate, the dimensionless injection parameter I is generally used. It is defined as the bleed mass flow rate normalized by the product of the base area and the freestream mass flux:

$$I = \frac{\dot{m}}{\rho_0 U_0 S_{\mathrm{base}}} \tag{8}$$

For the bleed temperature, the dimensionless temperature T_{bb}/T_0—where T_0 is the static temperature of the external flow and T_{bb} is the total base bleed temperature—is arbitrary employed.

4.2. Preliminary study

The numerical study of this case of reference, which started in a previous study [30], allows to show that computations are able to describe correctly the transition between the different bleed regimes (especially the two first ones) when the bleed mass flow rate is increased. To do that, the behavior of the base pressure p_c is examined (the flow analysis is made in the next section). Seven computations are performed with increasing bleed rate ranging from $I = 0$ to $I = 0.0226$. The total bleed temperature is fixed at the same value as the experiments i.e. $T_{\mathrm{bb}} = 300$ K ($T_{\mathrm{bb}}/T_0 = 2.26$).

4.2.1. Procedure to obtain a significant value of the base pressure

Here is described the methodology employed to extract a base pressure value from each computation. The base pressure, p_c, is the space-averaged value of the pressure acting on the annulus surface of the base. Considering $\vec{x}$ as the axial direction:

$$p_c = \frac{1}{S_{\mathrm{base}}} \|\vec{T}\|_{p_{\mathrm{base}}} = \frac{1}{S_{\mathrm{base}}} \int_{S_{\mathrm{base}}} -p\vec{n}\,\mathrm{d}S \cdot \vec{x} \tag{9}$$

For each bleed rate value, the unsteady computations lead to a quasi-steady solution. So, the base pressure is not a constant function of time but varies around a constant value. In the

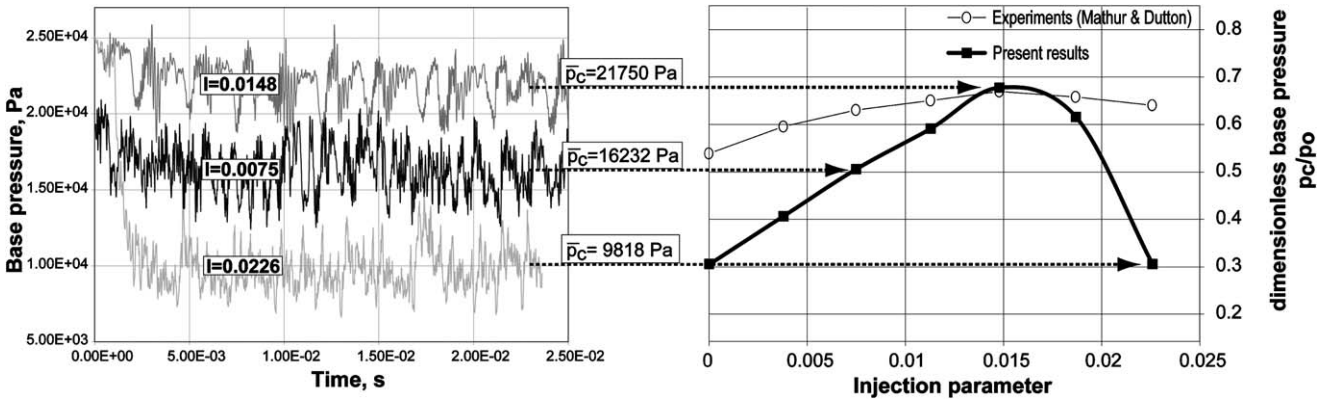

Fig. 4. Construction of the graph: Base pressure vs. injection parameter. Left: Temporal evolution of the base pressure signal p_c for three different bleed flow rates. Each base pressure signal is time-averaged; the obtained $\overline{p_c}$ value is plotted as a function of the bleed parameter I on the right. Experimental results from [19] are also shown.

left of Fig. 4, the time-evolution of the base pressure signal $p_c(t)$ for three computations using grid 2 with different bleed rates is shown: for each case, the base pressure signal is clearly unsteady, but a time-averaged value $\overline{p_c}$ of the base pressure signal can be extracted. Then, one can plot the dimensionless base pressure $\overline{p_c}/p_0$ (where p_0 is the upstream pressure; here $p_0 = 32094$ Pa) as a function of the bleed injection parameter (Fig. 4, right). In the following, the term "base pressure" is assumed to be the time-average value $\overline{p_c}$ of the base pressure signal, once the quasi-steady solution is attained. Concerning the temporal evolution of the base pressure signals, an analysis via FFT did not reveal any preponderant frequency.

Considering the behavior of $\overline{p_c}$ when injection parameter increases, experimental values and results from computations are plotted on the right of the Fig. 4. Numerical results show that the base pressure increases quasi-linearly with the bleed rate from $I = 0$ to $I = 0.0148$, which is a characteristic of regime I. The optimum bleed rate value ($I = 0.0148$) is in good agreement with experiments. Increasing bleed rate past this optimum decreases the base pressure: regime II has been reached. Transition between regime I and regime II is well simulated. One can notice disagreements between our calculations and the experiments in the level of the base pressure values, or, more precisely, in the variation of pressure inside each regime. Different causes may be suspected: mesh grid size, 3D effects, influence of the boundary conditions. Mesh grid size influence is investigated in the next paragraph. Three-dimensional mushroom type structures have been experimentally visualized [31] but, of course, cannot be simulated with the axisymmetric computations performed here. About boundary conditions, the supersonic conditions of the external flow cannot disturb the supersonic inlet boundary conditions. On the other hand, when flow conditions are locally subsonic, as in the trailing wake, outlet boundary conditions (if not well treated) may generate reflected acoustic waves which can disturb the flow near the base. This kind of problem has been anticipated. Numerous prospective computations, with varying computational domain geometry, were carried out before this study and did not show any influence of the outlet boundary condition on the time-averaged base pressure $\overline{p_c}$ or even on the base pressure signal

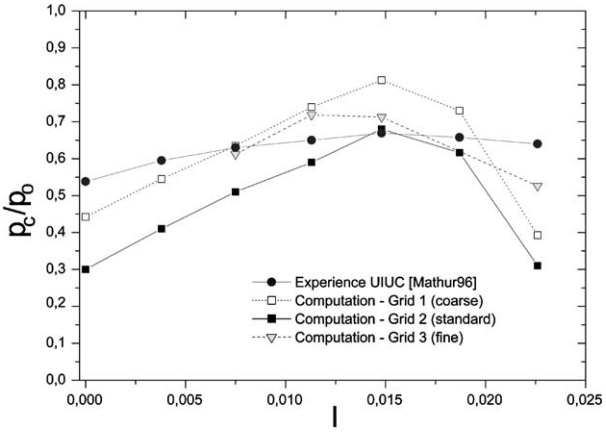

Fig. 5. Grid size effects—Base pressure vs. bleed rate (case of reference).

(as already said, no typical frequency of the base pressure signal could be connected to any length).

4.2.2. Grid size effects

The influence of the grid refinement has been investigated with three grids of decreasing cell size (described earlier). The case of reference $T_{bb}/T_0 = 2.26$ is still considered. Fig. 5 shows the evolution of the base pressure for the three grids of increasing cell number. Experimental data [6,7,29] are also plotted on the same Fig. 5.

Strong dependence of the numerical results with the mesh grid size is easily observable. The behavior of the base pressure vs. bleed flow rate, when increasing the cell number, is not simple. No solution has been found to be the "converged solution" in terms of mesh size: in our study, no cell size has been found to be the size under of which decreasing the cell size even further does not change the solution.

Some comments have to be made for which Fig. 6 is needed. The precise description of the flow features is not made here, but one can just notice that this figure represents the mass fraction contours of the bleed gas for the case $I = 0.0075$ and for the three grid used. Detached flows, as the ones studied in this paper, present strong instabilities which develop in the mixing

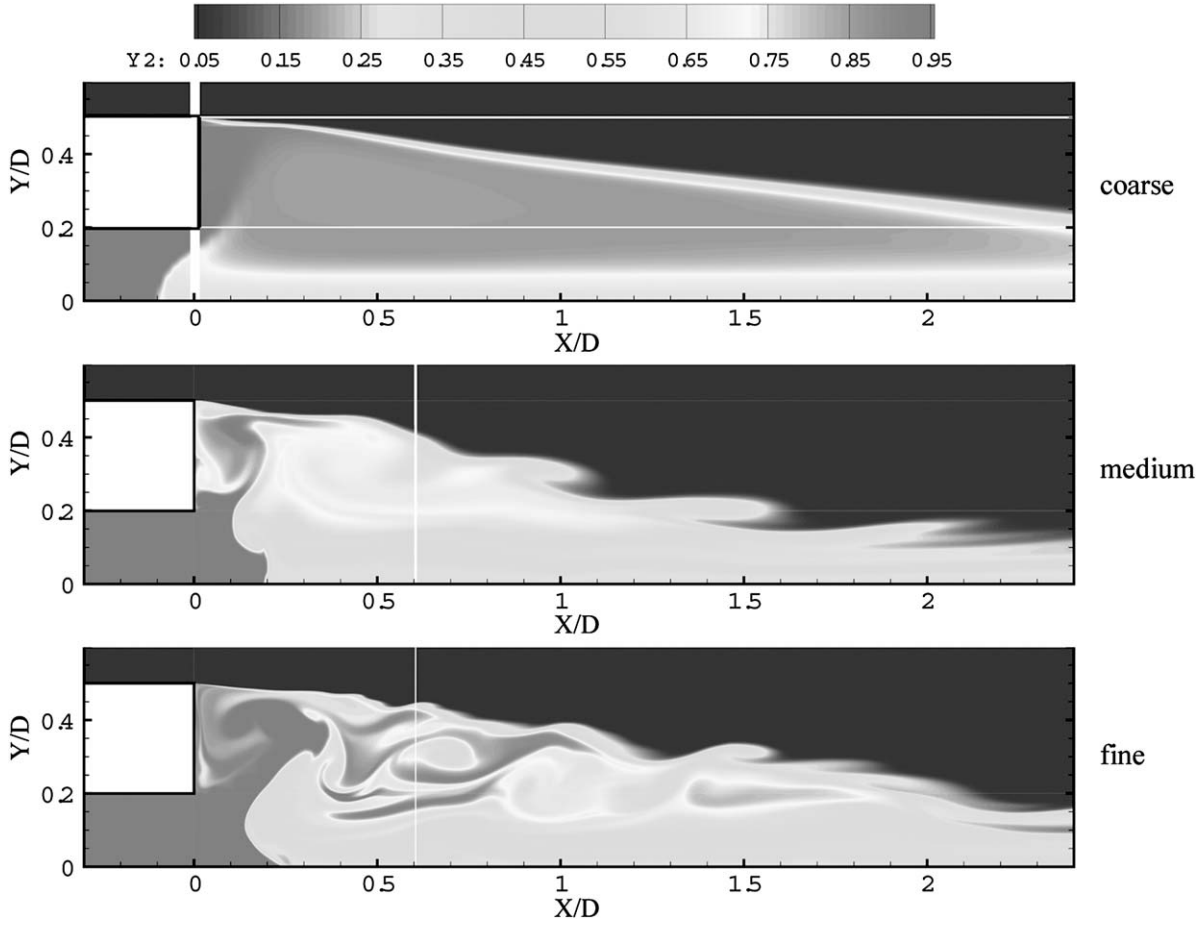

Fig. 6. Comparison of instantaneous contour of injected gas mass fraction for the case of reference, $I = 0.0075$, with the three grid used: grid 1 (top), grid 2 (middle) and grid 3 (bottom).

layers, grow and lead to fully turbulent flow in the base region. NS computations can simulate the largest scales of the instabilities present in the flow (Fig. 6, middle) but the smallest scales are not simulated (and erased by numerical viscosity) if the grid is too coarse (Fig. 6, top). For higher detailed mesh, lower scale instabilities are simulated as well in the mixing zones (Fig. 6, bottom), and quasi-steady solutions are evidently modified, besides base pressure level (Fig. 5). But, the typical spectrum of instabilities found in a turbulent flow, from the largest scales to the smallest, cannot be simulated until DNS is reached, which is not currently possible on this configuration (predict the 'real' flow behavior is then impossible nowadays). Thus, a highly detailed grid allows increasing the range of scale simulated, but a converged solution, in terms of mesh size, is not attainable with NS computations.

With a turbulence model, a converged solution (in term of mesh size) would certainly have been obtained: by increasing grid detail, which is necessary to obtain highest precision of the model (but a solution which still depend on the selected model), any small structure which tends to develop is destroyed by the artificial viscosity generated by the model himself. Furthermore, the lack of turbulence modeling is the most probable explanation for the difference between experimental and numerical values of base pressure. But, as said in the introduction, the lack of turbulent model able to describe correctly base flows is still one of the major problems of compressible CFD [17] and the authors, considering that the major point of this paper is to investigate a possible base bleed effect improvement by using metallic particles combustion, made the choice to not use any of the available models.

Finally, in the authors' opinion, the point of numerical simulations in this configuration is, in addition to describe the most of the features of the flow, to predict correctly regimes transition as from a regime to another, base pressure behavior is inverted. Our computations show that the transition between regimes I and II is well described with all of the three grids used: firstly, it occurs at the same bleed rate $I = 0.0148$ for each grid, and, secondly, the major features of the flow are present and relatively similar regardless of the grid used (see the presence and the length of the PRR in each case of Fig. 6). In order to obtain a minimum level of details, grid 1 is however discarded. The improvement in the description of the flow with grid 3, in comparison with grid 2, is not enough important (Fig. 6, bottom and middle) considering the much higher computational cost of grid 3. With grid 2, finally, even if quantitative results on base pressure should be taken with care, the major flow features which lead the transition mechanisms (like explained in Section 4.3.2.) can be well predicted. Grid 2 will be used afterwards for the extended one-phase study and the two-phase injection study.

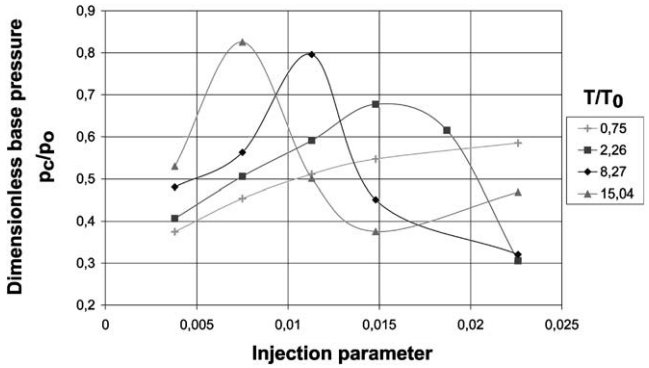

Fig. 7. Base pressure vs. injection parameter for several injection temperatures (grid 2).

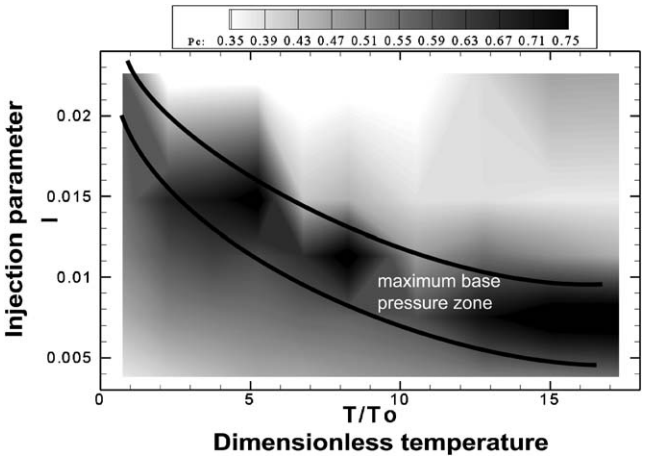

Fig. 8. Optimal bleed conditions.

4.3. Extended one phase study

4.3.1. Temperature effects

The influence of both the bleed mass flow rate and the bleed temperature is now investigated. The same method as previously is adopted but here, both bleed mass flow rate and bleed temperature can vary. Temperature values are chosen as follow: one value lower than the experimental case (100 K), and several values higher than the experiments from 500 K to 2300 K stepped by 200 K. The lower value is clearly not realistic but only a tendency is here researched. The considered bleed dimensionless temperature range is then 0.75–15.04. For each temperature value, six computations are performed with an increased injection parameter.

Fig. 7 summarizes the representative results of the entire temperature and bleed rate range. Like explained before, each point represents the time-averaged value $\overline{p_c}$ of the "quasi-steady" base pressure signal obtained during a computation.

Two major observations can be made. The first one is that the higher is the injection temperature, the lower is the mass flow rate where transition between regime I and II occurs: with $T/T_0 = 0.75$, the regime II is not reached even for the highest simulated bleed rate, then, with $T/T_0 = 2.26$, $T/T_0 = 6.77$ and $T/T_0 = 15.04$, transition is observed respectively at $I = 0.148$, $I = 0.0113$ and $I = 0.0075$. The second observation is that the maximum base pressure attained at the transition (optimal) bleed rate globally increases with bleed temperature ($(p_c/p_0)_{\max} = 0.68$, 0.79 and 0.82 for $T/T_0 = 2.26$, $T/T_0 = 6.77$ and $T/T_0 = 15.04$ respectively). Noticeably, regime III is reached for both maximum bleed rate and maximum temperature simulated ($T/T_0 = 15.04$ and $I = 0.0226$).

With all the base pressure values obtained with 60 computations (not all shown in the previous Fig. 7), the simple plot which represents the optimal bleed conditions both in temperature and mass flow rate can be constructed (Fig. 8). It shows base pressure levels (lower levels in white and higher levels in black) versus temperature in abscissa and injection parameter I in ordinate. Solid lines highlight maximum base pressure values and remind the previously observed balance between those two parameters that one has to take into account when optimizing the base bleed system. Also, best base bleed effect is found for lowest injection rates with highest temperatures.

4.3.2. Flow transition mechanism

Here, we focus on the flow changes occurring during the transition from regime I to regime II in order to verify that computations agree with the description of previous studies (see first section). The case of reference $T_{bb}/T_0 = 2.26$ is considered.

Figs. 9(a)–9(c) represent instantaneous contours of vorticity in the base region for three different bleed rates; the instant is chosen as the solution is representative of the quasi-steady solution. Zero vorticity level is gray. Fig. 9(a) shows the case $I = 0.0075$ which corresponds to regime I as seen in Fig. 4. The main characteristic of this regime is the primary recirculation region (PRR) which is clearly visible in the center of the Fig. 9(a). It is slightly detached from the base: the forward stagnation point is located at $x = 0.02$ m. The bleed gas is stopped by the PRR and deviated from the symmetry axis in the radial direction. Then it goes around the PRR trough the external mixing layer in which shear layer instabilities (Kelvin–Helmholtz instabilities) are visible. The secondary recirculation region (SRR), composed by two contra-rotative vortices against the base wall, shows reverse velocities higher than 2/3 of the upstream velocity. Maximum reverse velocity in the PRR is obviously on the axis and does not reach 2/3 of the upstream velocity.

Fig. 9(b) corresponds to the case $I = 0.0113$, which is the end of regime I (the optimal bleed rate is reached for $I = 0.0148$). Flow behavior is nearly the same as the previous case—the PRR is still present—excepted that the bleed jet is stopped farther (approx. one radius) from the base. Here, Kelvin–Helmholtz instabilities are also visible at the mixing layer between the bleed jet and the SRR. The SRR has increased both in length and strength. Maximum reverse velocities reach 3/4 of the upstream value.

In Fig. 9(c), regime II is attained as PRR is not present anymore. The bleed jet has enough momentum to prevent any reverse flow to develop on the symmetry axis. The higher bleed velocity leads to an increased length and strength of the SRR, in which the pressure is decreased enough to cancel the benefic base bleed effect observed in regime I.

It is important to note that the Mach number inside the bleed cavity and at the bleed exit is always subsonic, for all the

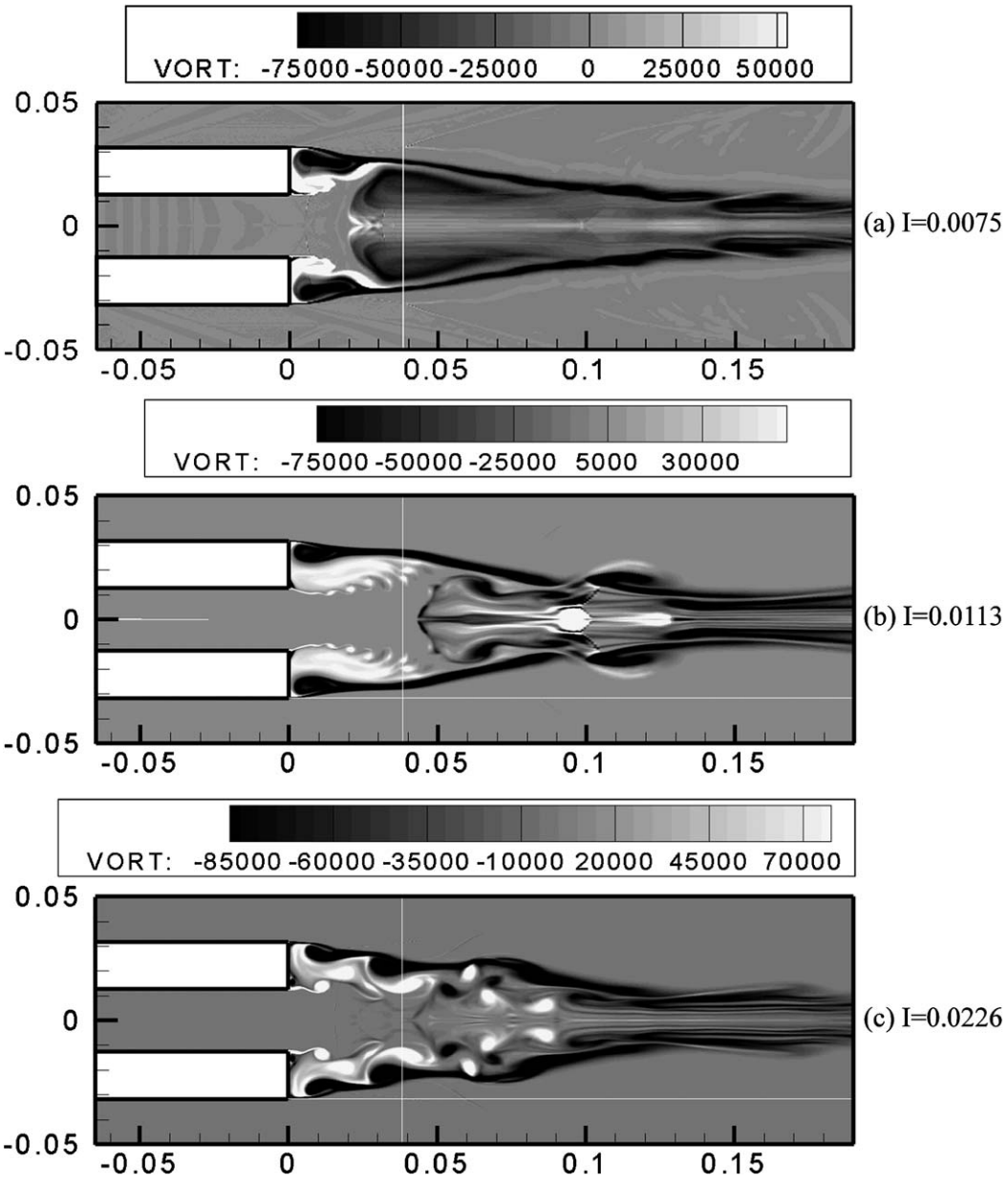

Fig. 9. Instantaneous contour of vorticity for: (a) regime I, (b) end of regime I and (c) regime II.

case corresponding to regime I and the beginning of regime II. Fig. 10 shows Mach number profiles at the bleed exit. The case $I = 0.0226$ shows locally supersonic zone on the edge of the jet.

4.4. Two-phase study

Previous paragraph has shown that the use of high temperature bleed gases increases the base bleed reducing drag effect. The best way to obtain a high temperature (>2000 K) of gases produced by the combustion of a propellant is to add reactive metal particles into its composition. Indeed, the aluminum particles combustion, that we are interested with, leads to high energy transfers between the particles and the gas.

Two-phase reactive computations have been achieved and a sensitive increase of the base pressure has been obtained thanks to the reactive particles added to the bleed injection. One has to notice that the Eulerian approach and the combustion model have been successfully applied to this axisymmetric external configuration, which is not a trivial problem. Indeed, several numerical difficulties, some of which are described further, had to be resolved before obtaining realistic results.

Hereafter, the combustion effects are pointed out and the two-phase reactive flow is analyzed on a particular case, which is an extension of the optimal case of the previous one-phase study.

4.4.1. Flow conditions

Same external flow conditions as the previous section are considered. Concerning the base bleed injection, it represents a typical mixture produced by an aluminum loaded propellant: hot gases and 10 μm diameter aluminum particles (Fig. 11).

The mass rate of aluminum particles in the injection is taken at 15%. Typical values for the temperature of gases and particles coming from the combustion of a propellant are respectively $T_g = 2100$ K and $T_p = 2767$ K. The chosen case is the case where maximum base pressure ($p_c/p_0 = 0.82$) has been reached for this bleed gas temperature in the previous one-phase study: $I = 0.0075$.

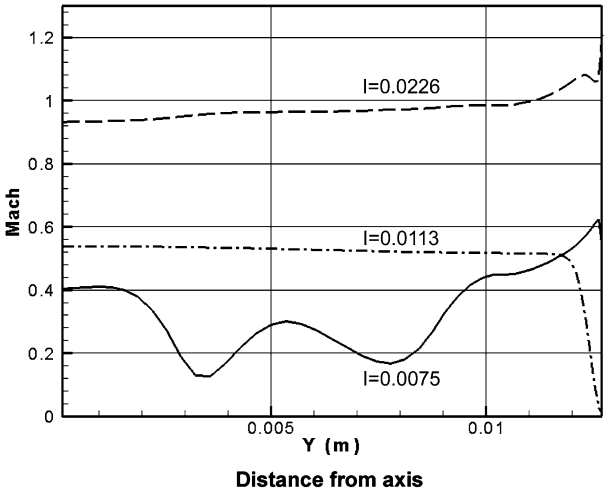

Fig. 10. Mach number profiles at the bleed exit.

Concerning the gas phase, a lot of species are present in the injected combustion mixture; they are classified in two groups depending on their reactivity with the metal particles: the inerts (I) and the oxidizers (OX). A third group represents the combustion products (PC). The external flow is considered as a typical O_2, N_2 mixture. Particles can react with (OX) from the injection and/or O_2 from the external flow.

Concerning the particles, as already specified, two species are present: aluminum (Al) first, and alumina (Al_2O_3) as a solid combustion product condensed on the particles surface. The thermodynamic characteristics of these two materials are gathered in Table 1.

4.4.2. A sensitive increase of base pressure

Thanks to the energy released in the base region by the combustion process, the base pressure reaches a higher value than

Table 1
Thermodynamic characteristics of aluminum and alumina materials

Aluminum vaporization heat	$l_{VAP} = 10896 \times 10^3$ kJ kg^{-1}
Aluminum saturation temperature	$T_{SAT} = 2767$ K
Aluminum density	$\rho^*_{Al} = 1766$ kg m^{-3}
Alumina density	$\rho^*_{Al_2O_3} = 2513$ kg m^{-3}
Liquid aluminum specific heat	$Cp_{Al} = 1176$ J kg^{-1} mol^{-1}
Liquid alumina specific heat	$Cp_{Al_2O_3} = 1418$ J kg^{-1} mol^{-1}

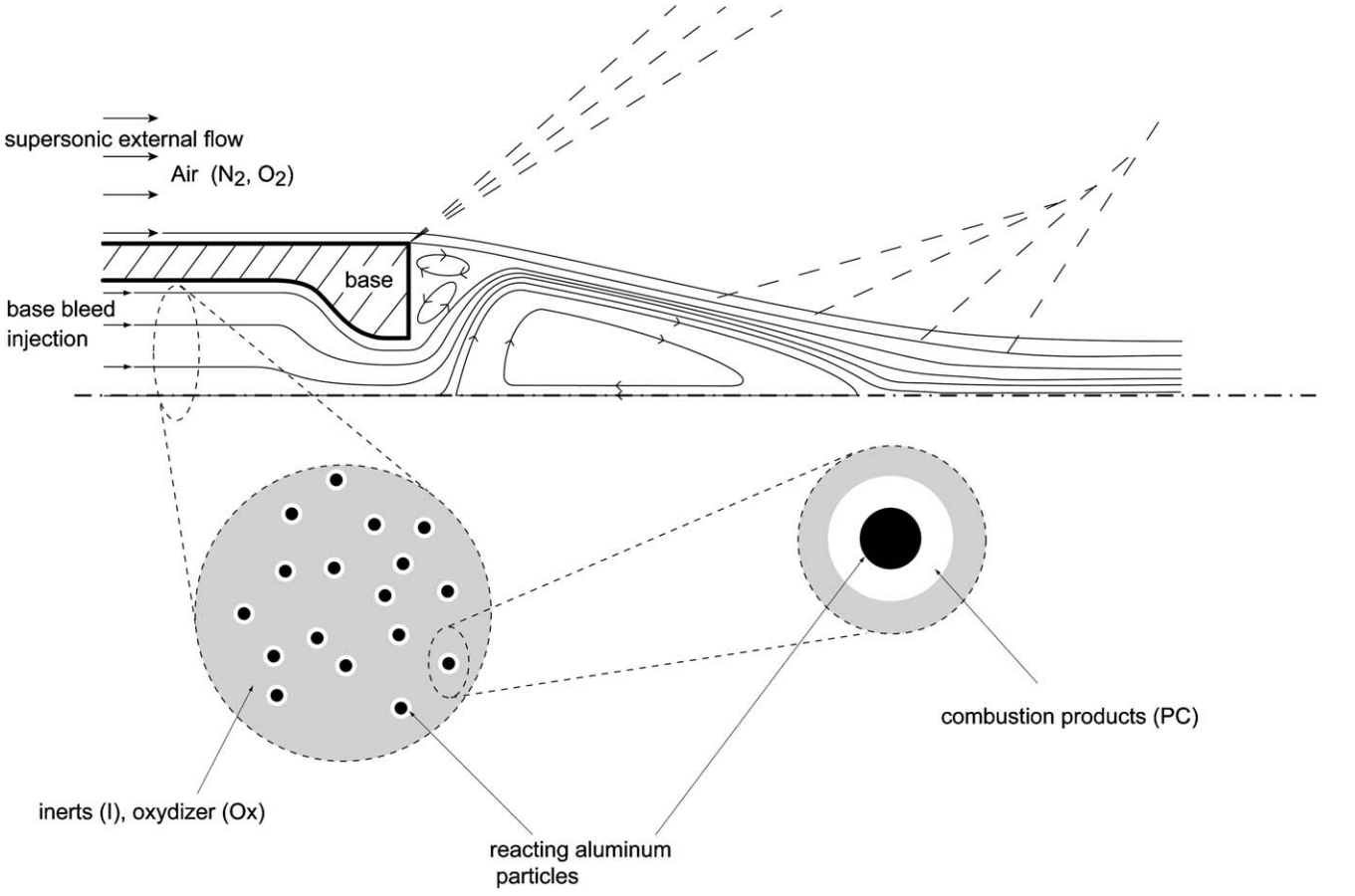

Fig. 11. Sketch of the two-phase reactive injection case.

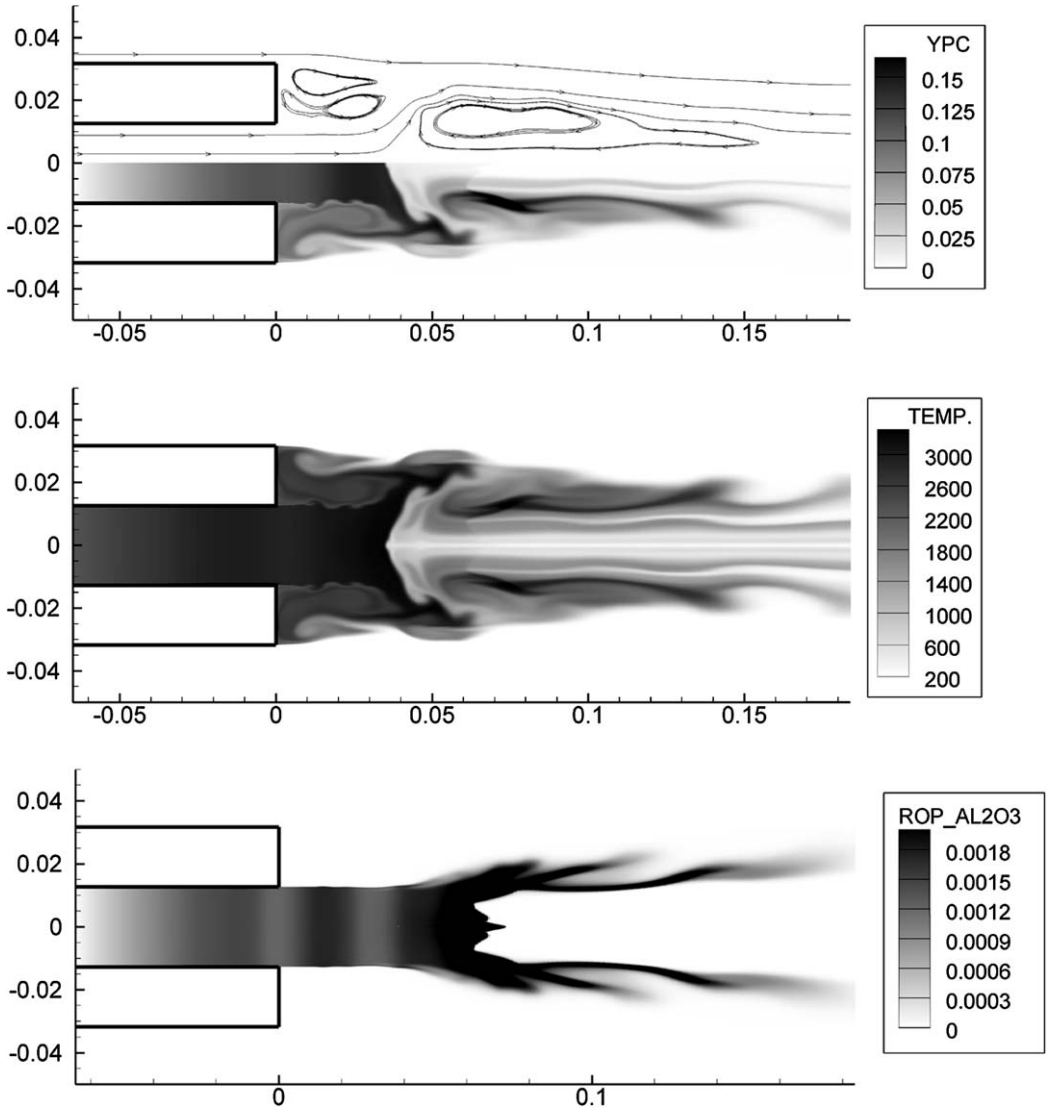

Fig. 12. Streamtraces of the gaseous phase and mass fraction contour of combustion products (top), contour of gas temperature (middle) and contour of alumina density (bottom).

all previous computations: $p_c/p_0 = 0.87$. In the following, the two-phase reactive flow is analyzed using Figs. 12 and 14 which are, at the same time, instantaneous contours of several characteristics of each phase.

Fig. 12 (top) shows the mass fraction contours of the gaseous combustion products and also the streamtraces of the gaseous phase. Combustion products are evidently not present at the bleed boundary but appear progressively along the bleed section showing the effectiveness of the combustion process. These products are massively accumulated in the front of the PRR, which is pointed out by the streamtraces in Fig. 12 (top). As seen before, the presence of the PRR is a characteristic of regime I, then the gas flow behavior is typical of this regime: gaseous combustion products, and also inerts and oxidizers, are stopped on the symmetry axis by the reverse flow of the PRR; they go around the PRR trough the mixing layer before escaping in the wake.

Fig. 12 (middle) shows contours of gas temperature. High gas temperature levels are reached thanks to combustion energy transfers ($T_{\max} = 3200$ K) near the forward stagnation point of the PRR. Convective mixing leads to nearly 2700 K in the SRR. These high temperature levels near the base surface are certainly the reason of the high base pressure value observed.

Fig. 12 (bottom) shows contours of alumina density $\rho_{Al_2O_3}$. Alumina is the solid combustion product condensed on the particle. Alumina mass fraction increases along the bleed section as a result of the combustion of particles with the bleed gas which contains oxidizers. Alumina mass fraction increases again in the base region where the particles react both with oxidizers from the bleed gases and the oxygen from air. High alumina mass fraction levels in the near wake region are due to particles accumulation and not to higher combustion rate.

One can note that the solid and the gaseous combustion products contours are not identical: even if the two phases are described by two coupled equation systems, the particles inertia allows them to have a motion different from gas. Particles penetrate through the PRR and are stopped on the symmetry axis inside of the PRR (≈0.06 m from the base) by the re-

verse gaseous flow. They are then radially deviated and forced to escape in the wake dropping by the gaseous external mixing layer. This motion leads to an important feature of this two-phase flow: the presence of a no particle zone in the core of a two-phase flow.

This is a particularity that our numerical procedure has to describe correctly. This is also true for the treatment of the two-phase zone/no-particles zone interfaces. Another difficulty is the existence of local high particles density zones, principally at the dispersed phase stagnation point (Fig. 13). These zones lead to high heat and mass transfers (transfers due to combustion are evidently proportional to the number of particles) which increase the risks of numerical divergence. Let us remind that the Eulerian description of the particles dynamics assume a "dispersed" media. A high particles density zone could locally make this assumption not valid. To prevent this problem and to correctly describe these zones, a particles diffusion model [32], which takes into account the particles interaction, is locally used. It modifies Eqs. (4) and (7) respectively as follow:

$$\frac{\partial \rho_p \vec{U}_p}{\partial t} + \vec{\nabla}.(\rho_p \vec{U}_p \vec{U}_p - \bar{\bar{\tau}}_p) = -\vec{F}_{g-p} - \Gamma_m \vec{U}_p \tag{10}$$

$$\frac{\partial \rho_{p,i}}{\partial t} + \vec{\nabla}.(\rho_{p,i} \vec{U}_p - D_p \vec{\nabla}.\rho_{p,i}) = -\dot{\Gamma}_{p-g,i} + \dot{\omega}_{p,i} \tag{11}$$

where $\bar{\bar{\tau}}_p = \mu_p(\vec{\nabla}\vec{V}_p + (\vec{\nabla}\vec{V}_p)^{\mathrm{T}}) - \frac{2}{3}\mu_p(\vec{\nabla}\vec{V}_p\delta_{ij})$ is the stress tensor of the dispersed phase. μ_p and D_p are respectively the particulate diffusion coefficient and the particulate viscosity.

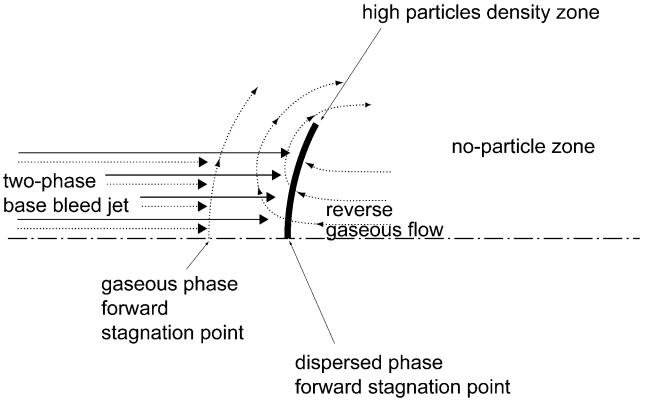

Fig. 13. Difficulty for the Eulerian description of a two-phase base bleed injection.

The values $\mu_p = 10^{-2}$ kg m^{-1} s^{-1} and $D_p = 10^{-3}$ s^{-1} are used here.

Fig. 14 shows the diminution of the particles diameter, from 10 μm at the bleed inlet boundary to nearly 9 μm at the bleed section, and to nearly 7.5 μm at a distance of 0.2 m downstream from the base. This diminution is obviously due to particles combustion. The combustion process is not finished yet in the observed domain as the particles temperature contours (not shown) shows a constant temperature of 2767 K everywhere particles are present: indeed the particles temperature is imposed equal to the aluminum saturation temperature during all the combustion process.

4.4.3. Two-phase inert injection & real combustion effects

Some comments have to be done to show that the observed gain on base pressure is due to the reactivity of the particles and not only to the presence of particles themselves. Indeed, the presence of inert particles in the injection tends to decrease base pressure levels in regime I and also when regime II is reached (as shown on the Fig. 15, for the case of reference). This phenomenon can be explained by the fact that particles movement is leaded by drag forces acting on the particles: the particles motion needs momentum transfer from the carrying phase to the dispersed phase. The injected gas undergoes a loss of energy which is no longer available for the base bleed effect. Optimal bleed rate is found to be the same as the one-phase injection case, but maximum base pressure is decreased by more than 25% (Table 2).

Concerning the chosen case for the reactive two-phase injection (corresponding to the optimal conditions of the one-phase study), an inert two-phase computation has been carried out in order to highlight the combustion effects. It uses similar conditions but the combustion source terms are turned off. In this last case, the base pressure value is lower than the one-phase corresponding case (8.5% less), even if heat transfers occur between the hot particles and the carrying phase. The presence of particles leads to a loss of momentum for the gaseous phase that the convective heat transfer cannot compensate. The base pressure value is also lower than the two-phase reacting case (13.8% less). Base pressure values obtained for these three cases are regrouped in Table 3.

The gain on base pressure may appear low regarding to the increased difficulty to obtain aluminum loaded propellants,

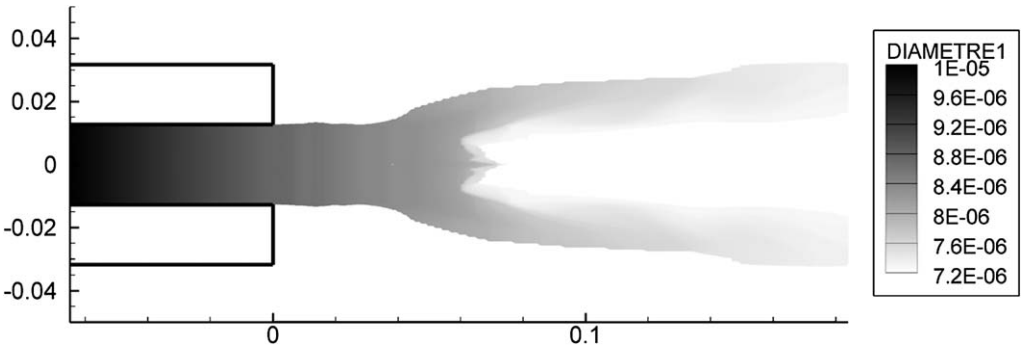

Fig. 14. Contour of particle diameter.

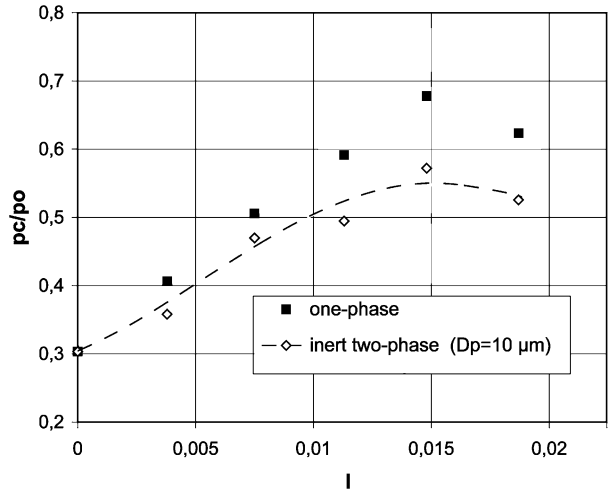

Fig. 15. Base pressure decrease when two-phase inert injection is considered (case of reference).

Table 2
Base pressure values for a one-phase and a two-phase inert injection (optimal conditions of the case of reference $I = 0.0148$)

Injection type	One-phase	Two-phase
T_g^{inj} [K]	300	300
T_p^{inj} [K]	–	300
$(p_c/p_0)_{\max}$	**0.68**	**0.50**

Table 3
Base pressure values for one-phase, two-phase inert and two-phase reacting case (optimal hot injection case $I = 0.0075$)

Injection type	One-phase	Two-phase inert	Two-phase reactive
T_g^{inj} [K]	2100	2100	2100
T_p^{inj} [K]	–	2767	2767
$(p_c/p_0)_{\max}$	**0.82**	**0.75**	**0.87**

however, such gas temperature levels cannot be reached easily without metallic particles addition.

5. Conclusion

First, the one-phase study has shown the capacity of our computations to describe the flow transition between the two first bleed regimes (regime III is also well predicted but out of the topic of the present paper). Transition occurs when the bleed injection provide enough momentum and/or energy to the detached flow in the base region. Coupled effects of bleed mass flow rate and bleed gas temperature has been analyzed. The optimal conditions for base bleed have been shown to occur both for lower injection mass flow rate and higher bleed temperature.

Then, the best way to obtain high temperature for gases usually injected from the combustion of a propellant is to add metallic load to the propellant composition. Two-phase reactive unsteady computations have been achieved and have shown that very high temperature levels could be attained thanks to high energy provided to the gas by the aluminum particles combustion process.

Acknowledgements

The authors would like to thank Paul Weinacht, from the Army Research Laboratory Proving Ground, and Georges Le Palec, from the Ingénierie en Mécanique des Fluides et Thermique research team in Marseilles, for useful discussions.

References

[1] D.R. Chapman, An analysis of base pressure at supersonic velocities and comparison with experiment, NACA Report 1051 NACA Technical Note 2137, 1951. Available at http://naca.larc.nasa.gov/reports/1951/naca-report-1051/.
[2] J. Delery, M. Sireix, Ecoulements de culot, AGARD Lecture Series, No. 98, February 1979.
[3] J. Delery, ONERA research on afterbody viscid/inviscid interaction with special emphasis on base flows, in: Proceedings of the Symposium on Rocket/Plume Fluid Dynamics Interaction, University of Texas at Austin, 1983.
[4] J.L. Herrin, J.C. Dutton, Supersonic base flow experiments in the near wake of a cylindrical afterbody, AIAA Journal 32 (1994) 77–83.
[5] J.L. Herrin, J.C. Dutton, Effects of afterbody boattailing on the near-wake of axisymmetric bodies in supersonic flow, in: 32nd Aerospace Science Meeting and Exhibit, January 10–13, 1994, Reno, NV.
[6] T. Mathur, J.C. Dutton, Base bleed experiments with a cylindrical afterbody in a supersonic flow, Journal of Spacecraft and Rockets 33 (1996) 30–37.
[7] T. Mathur, An investigation of the effects of base bleed in axisymmetric supersonic flow, PhD thesis, Department of Mechanical, University of Illinois at Urbana-Champaign, 1996.
[8] H.H. Korst, A theory for base pressures in transonic and supersonic flow, Journal of Applied Mechanics 23 (593) (1956).
[9] R. Benay, P. Servel, Two-equation turbulence model: Application to a supersonic base flow, AIAA Journal 39 (3) (2001).
[10] S. Deck, E. Garnier, P. Guillen, Turbulence modelling applied to space launcher configurations, Journal of Turbulence 3 (2002).
[11] J. Sahu, C.J. Nietubicz, J.L. Steger, Navier–Stokes computations of projectile base flow with and without mass injection, AIAA Journal 23 (1985) 1348–1355.
[12] J. Sahu, K.R. Heavey, Numerical computations of supersonic base flow with special emphasis on turbulence modeling, AIAA Journal 32 (1994) 47–49.
[13] J. Sahu, K.R. Heavey, Numerical investigation of supersonic base flow with base bleed, Journal of Spacecraft and Rockets 34 (1997) 62–69.
[14] J. Sahu, R. Heavey, Numerical investigations of supersonic base flow with base bleed, Journal of Spacecraft and Rockets 34 (1) (1997) 62–69.
[15] J.R. Forsythe, K.A. Hoffman, R.M. Cummings, K.D. Squires, Detached-eddy simulation with compressibility corrections applied to a supersonic axisymmetric base flow, Journal of Fluids Engineering 124 (2002).
[16] R. Paciorri, F. Nasuti, F. Sabetta, Evaluation of turbulence modeling in supersonic afterbody computations, AIAA-paper, 2001, pp. 2001–3039.
[17] R. Benay, B. Chanetz, J. Delery, Code verification/validation with respect to experimental data banks, Aerospace Science and Technology 7 (2003) 239–262.
[18] C. Fureby, Y. Nilsson, K. Andersson, Large eddy simulation of supersonic base flow, Technical Report, FOA Defense Research Establishement, Weapons and Protection Division, 147 25 Sweden, February 1999.
[19] P. Kaurinkoski, Simulation of the flow past a long-range artillery projectile, PhD thesis, Helsinki University of Technology, 2000, URL: http://lib.hut.fi/Diss/2000/isbn951225199X/.
[20] P. Kaurinkoski, A. Hellsten, Numerical simulation of supersonic base-bleed projectile with improved turbulence modelling, Journal of Spacecraft and Rockets 35 (5) (1998) 606–611.
[21] I. Rose, J. Vos, A. Gheri, Flow calculations of spinning base bleed shell, in: Proceedings of the 20th International Symposium on Ballistics, Orlando, USA, 2002.

[22] I. Rose, J. Vos, A. Gheri, Drag reduction through after-burning of base-bleed gases, in: Proceedings of the 21st International Symposium on Ballistics, Adelaide, South Australia, 19–23 April 2004.

[23] H. Forconi, C. Masson, Générateur de gaz liant fluor pour obus réduction de trainee, in: Proceedings of the RTO—AVT Panel Meeting Workshop, Corfou (Grèce), 19–23 Avril 1999.

[24] E. Daniel, Eulerian approach for unsteady two-phase reactive solid rocket motor flows loaded with aluminum particles, Journal of Propulsion and Power 16 (2000) 309–317.

[25] T. Basset, E. Daniel, J.C. Loraud, Etudes numériques et théoriques sur la combustion de particules d'aluminum, Canadian Journal of Chemical Engineering 75 (1997) 938–948.

[26] N. Thevand, E. Daniel, On high resolution schemes for solving unsteady compressible two-phase dilute flows, International Journal for Numerical Method in Fluid 35 (10) (1999) 1789–1871.

[27] N. Thevand, E. Daniel, Linear instability of dilute particle-laden compressible mixing layer, Physics of Fluids 14 (2002) 392–402.

[28] R. Saurel, E. Daniel, J.C. Loraud, Two-phase flows: second order schemes and boundary conditions, AIAA Journal 32 (1994) 1214–1221.

[29] T. Mathur, J.C. Dutton, Velocity and turbulence measurements in a supersonic base flow with mass bleed, AIAA Journal 34 (1996).

[30] H. Bournot, E. Daniel, G. Le Palec R. Cayzac, Numerical simulation of base-bleed effect in a supersonic flow over a cylindrical afterbody, in: Proceedings of the 21st International Symposium on Ballistics, Adelaide, South Australia, 19–23 April 2004, vol. 1, pp. 485–491.

[31] C.J. Bourdon, J.C. Dutton, Planar visualizations of large-scale turbulent structures in axisymmetric supersonic separated flows, Physics of Fluids 11 (1999) 201–213.

[32] A.J. Chamkha, J. Peddieson Jr, Boundary layer flow of a particulate suspension past a flat plate, International Journal of Multiphase Flow 17 (1991) 805–808.